

Dynamics of Rapidly Rotating Bose-Einstein Quantum Droplets

Szu-Cheng Cheng,¹ Yu-Wen Wang,² and Wen-Hsuan Kuan^{2,*}

¹*Department of Physics, Chinese Culture University,*

Yang-Ming-Shan, Taipei 11114, Taiwan.

²*Department of Applied Physics and Chemistry,*

University of Taipei, Taipei 10048, Taiwan.

(Dated: October 10, 2023)

Abstract

This work theoretically investigates the stationary properties and the dynamics of the rotating quantum liquid droplets confined in a two-dimensional symmetric anharmonic trap. Mimicking the quantum Hall systems, the modified Gross-Pitaevskii equation with the inclusion of the Lee-Huang-Yang nonlinear interaction is analytically solved, and the role of the Landau-level mixing effect is addressed. Via controlling the nonlinear interaction and the rotation speed, the rotating quantum droplet with multiply quantized vortex can be created, and the preference of the energetically favored quantum states can be distinguished in the phase diagram. To better interpret the underlying physics of the phase singularities, a brief comparison of the rotating quantum droplet and the optical vortex is made. The investigation of the long-term evolution of the rotating quantum droplets confirms the stability of the quantum states. At certain rotation speeds, the multi-periodic trajectories and breathings provide evidence of the emergence of the collective excitation of the surface mode in the vortex state. For quantum droplets carrying multiply quantized vortex, the microscopic snapshots of the rotation field adjusted current density distribution show that the combined nonlinear interaction and the anharmonic trapping potential can provide the restoring force to lead the quantum droplet to a regular and stable revolution and reach the dynamic equilibrium, revealing the signature of the generation of superfluids in the new kind of low-dimensional quantum liquids.

I. INTRODUCTION

Using laser cooling and trapping techniques, experimentalists can create atomic quantum gases at extremely low temperatures. Governed by the Bose-Einstein statistics, the emergence of the quantum phase transition and the realization of Bose-Einstein condensation below a critical temperature reveal the consequence of the quantum statistical effects. Applying the grand canonical ensemble theory, the critical temperature can then be defined by calculating the phase space filling at zero chemical potential. Having the same quantum configuration and sharing almost the same energy state, the macroscopic collection of cold atoms with a nonzero off-diagonal long-range order forms the Bose-Einstein condensates (BECs) [1–3]. With the mean field (MF) approximation, the dynamics of the BECs with weak interatomic interactions can be adequately described through the application of

* wenhsuan.kuan@gmail.com

the Gross-Pitaevskii equation (GPE). Near the Feshbach resonance, where the elastic scattering can be dramatically altered by an external field [4–6], a quasibound molecule can tunnel across a potential energy barrier and resonantly couple with the free states of the colliding atoms. Therefore, the possibility of tuning the magnitude and sign of the scattering length with external magnetic fields provides new perspectives on the manipulation of BECs [1, 7, 8].

Concerning the two-body interactions between a monatomic ensemble, an equilibrium between attractive interatomic forces and short-range repulsion due to the van der Waals forces will lead to the formation of a liquid in the cooling processes instead of a gas. Because of the high density and incompressibility, the attempts by usual liquids to enter the quantum regime are prohibited. However, with the inclusion of the Lee-Huang-Yang (LHY) correction to the ground state energy of a homogeneous weakly repulsive Bose gas [9], a new type of quantum liquid which emerges in the ultracold and extremely dilute atomic systems, violating the van der Waals model, has recently been observed in the two-component Bose mixtures [10–12] and single-component dipolar condensates [13–16]. Above the particle number threshold, the gas-to-liquid phase transition takes place when the instabilities arising from attractive mean-field interaction $\propto n^2$ are compensated for by the high-order quantum many-body effects, $\propto n^{5/2}$ [17]. By tuning the interatomic interactions, the realization of the dilute and weakly interacting self-bound liquid droplets provides direct evidence of the beyond MF effects [18].

Being a paradigm for quantum liquids, the superior coherence of the Bose superfluids is demonstrated by calculating the one-body density matrix and the correlation function between any two particles. To describe them, the introduction of the order parameter along with the low-lying elementary excitations obtained from the solutions to the Bogoliubov equations manifest the essence of the quantum fluctuations in the quantum phase transitions. For spinless atomic gases, the gradient of the phase of the condensate wavefunction defines the superfluid velocity, which is irrotational unless there is a singularity embedded in the phase of the order parameter such that the Onsager-Feynman quantization condition is satisfied. Through laser-stirred phase imprinting, the generation of vortex cores [19, 20], vortex rings [21, 22], and even vortex lattices [23, 24] in rapidly rotating dilute-gas BECs has been experimentally realized. In tightly trapped BECs, the formation of multiply quantized vortices and long-lived vortex aggregations has also been observed [25, 26], showing the

crucial influence of the Coriolis forces in the rotating systems.

Contrary to the gaseous BECs, the theoretical analysis has demonstrated that the quantum droplets of singly charged vortex states are unstable in the single-component dipolar condensate [27, 28]. However, it was reported that via analyzing the linearized Bogoliubov-de Gennes equations, stable solutions can be theoretically found for the 2D quantum droplets (QDs) with hidden and explicit vorticity [29], and for the 3D binary condensates with contact and LHY-amended interactions [30]. It has also been experimentally shown that the application of optical lattices helps to stabilize zero-vorticity and vortical solitons [31], whenever the Vakhitov-Kolokolov criterion can be violated in the vortex lattice QDs [32]. In the presence of the rotating field, the vortex lattices can be theoretically formed in a Gaussian-like QD [33]. Within harmonic confinement, a recent simulation reported that a self-bound and visible triangular vortex lattice can be formed without melting for a rotating QD in the quantum Hall limit [34]. These studies show that since the nonlinear competitions depict the domain boundaries for the vortex rings of a spinning droplet, the particle number for systems where the finite size effects are relevant is critical to the formation of the low-energy modes. The presence of the lattice potential restricts the axisymmetric solutions and breaks the spatial uniformity, isotropy, and the conservation of the linear and angular momenta.

Just as the neutral superfluids can be induced by rotation, charged superfluids can be initiated by a magnetic field. It is interesting that the system of an electron confined to two dimensions subjected to a perpendicular magnetic field is a harmonic oscillator problem in disguise. In this system, the electron kinetic energy is quantized, and the discrete energy levels are termed the Landau levels. In the strong magnetic field regimes, the occupation of the lowest Landau level (LLL) may occur, whereas the presence of interactions and disorders may stimulate the excitation to the higher Landau level states, resulting in Landau level mixing (LLM), which is prominent for a strictly 2D system since the primary contribution due to the short-range interaction is more effective with the decreasing thickness. From this point of view, the integral quantum Hall effect that exhibits the quantized Hall resistance plateaus and the Arrhenius behavior in the longitudinal resistance [35, 36] is a direct consequence of the Landau level formation. For the fractional quantum Hall systems, the introduction of Laughlin's theory and the composite fermion principle provide crucial clues to explore some novel phenomena such as skyrmions and fractional statistics [37–39]. Sharing many similarities, the application of the same mathematical formalism on the systems

of the charged particles in the strong magnetic field and the rotating neutral atoms has successfully predicted the bosonic Laughlin state [40, 41]. Some novel phenomena, such as the emergence of the incompressible states, the bosonic analog of the Jain sequence [42], and Abelian and non-Abelian states [43, 44], have been extensively explored in the past decade. In addition, the formation of exotic states in the case of rotating spinor bosons has also been studied [45]. In recent years, the realization of the geometric squeezing into the LLL of BECs and the interaction-driven spontaneous crystallization offers a new route towards strongly correlated fluids and bosonic quantum Hall states [46, 47]. While the discovery of the quantum Hall effects has revealed remarkable macroscopic quantum phenomena related to topological investigations for vortices, the known stable topological solitons, for example, the systems of rotating BECs with multiple degrees of freedom of tunable parameters, are versatile and can be promising for the topological quantum computations [48].

The objective of this work is to theoretically investigate the dynamics of a 2D rapidly rotating QD confined in a symmetric anharmonic trap. In the presence of the rotation field, the radial confinements are reduced by the centrifugal potential, and the Coriolis force experienced by the droplets in the rotating frame would appear equivalent to the Lorentz force on a charged particle. As the analogy between the quantum Hall effects and the rapidly rotating BECs in dilute gases has been precisely recognized, it will be interesting to see whether the artificial Lorentz forces can also be engineered for the new type of quantum liquids such that the generation of exotic phases carrying multiple topological charges can be observed, the route for the quantum phase transition can be depicted, and the singularity and the stability of the quantum states can be managed in this system. These explorations would make it possible to simulate the quantum Hall-type effects in a controlled manner with low-dimensional nonuniform quantum liquids. Since the combined effect of interactions and quantum statistics will eventually determine the features of the many-body ground state, such rotating systems, therefore, allow us to study the artificial orbital magnetism in quantum liquids.

The article is organized as follows. In Sec. II, we present the details of the application of the LHY correction to calculating the interatomic potential energy and the energy density of a 2D self-bound QD. In Sec. III, with the inclusion of the LLM effect, we present the analytic solutions of the LHY-amended GPE for an anharmonically trapped rotating QD utilizing the variational method. We analyze the stationary properties including the density

profiles and the phase distributions in III.A. To better interpret the underlying physics of the phase distributions, a brief comparison of the rotating QD and the optical vortex is made in III.B. The influences of nonlinear interaction and the rotation speed on the ground state configuration are demonstrated via the phase diagram in III.C. To avoid collapse from the three-body collisions and numerical divergence, a formulation for the maximum circulation restriction is proposed based on the LLL approximation. In Sec. IV, we further investigate the dynamics of the rotating QD. By solving the Euler-Lagrange equations, we analyze the periodicity and the stability of the QD under a linear perturbation in IV.A, and depict the probability current density distribution taken for a long-term evolutionary quantum state in IV.B. Finally, we summarize this work in Sec. V.

II. NONLINEAR INTERACTION AND ENERGY DENSITY: THE LEE-HUANG-YANG CORRECTION

In extremely low temperatures, the mutual interactions between ultra-dilute gaseous atoms are known to be well described in terms of the hard-core model and the s-wave scattering length. However, the situation becomes more complicated for the low-dimensional liquid systems, despite the fact that the 3D s-wave scattering lengths a^{3D} and $a_{\uparrow\downarrow}^{3D}$ adopted by Refs. [12] and [49] can be chosen for suitably describing the liquid-like droplet regimes.

To form a 2D quantum droplet in the system of dilute Bose-Bose mixtures with densities n_{\uparrow} and n_{\downarrow} , a weakly attractive interaction for the interspecies and a weakly repulsive interaction for the intraspecies are required. It has been proven that by writing the short-range interaction in terms of the coupling constant $\tilde{g}_{\sigma\sigma'}$ and the scattering length $a_{\sigma\sigma'}$ via $\tilde{g}_{\sigma\sigma'} = (4\pi\hbar^2/M)/\ln(4e^{-2\gamma}/a_{\sigma\sigma'}^2\Delta)$, where γ is the Euler constant and Δ is chosen such that $\tilde{g}_{\uparrow\downarrow}^2 = \tilde{g}_{\uparrow\uparrow}\tilde{g}_{\downarrow\downarrow}$, the weakly interacting regime beyond the MF approximation can be theoretically approached [50, 51] using the scattering t matrix [52]. For the symmetric case $a_{\uparrow\uparrow} = a_{\downarrow\downarrow} = a$ and $n_{\uparrow} = n_{\downarrow} = n$, the calculation of the energy density of a uniform liquid within the assumption of a macroscopic condensate population gives $E_{2D} = (4\kappa\hbar^2n^2/M)\ln(e^{2r+1/2}\kappa aa_{\uparrow\downarrow}n)$, in which $\kappa = 2\pi/\ln(a_{\uparrow\downarrow}/a)$, revealing the nonlinear LHY correction to the MF approximation. It can be further simplified to $E_{2D} = (2\kappa^2\hbar^2n^2/\pi M)\ln(n/en_0)$ by introducing the equilibrium density $n_0 = e^{-2r-3/2}/\kappa aa_{\uparrow\downarrow}$ for each component.

Referring to Ref. [50] for practical calculations, the 2D scattering lengths a and $a_{\uparrow\downarrow}$ would take the form of $a = l_z \exp[-\sqrt{\pi/2} l_z/a^{3D}]$ and $a_{\uparrow\downarrow} = l_z \exp[-\sqrt{\pi/2} l_z/a_{\uparrow\downarrow}^{3D}]$, respectively, where $l_z = \sqrt{\hbar/2M\omega_z}$ is the oscillator length in the strong confinement direction. In this work, the dynamics of a rotating QD is investigated by simulating a symmetric mixture of a quasi-2D ^{39}K self-bound oblate droplet [10]. We assume $\omega_z = 2\pi \times 400 \text{ Hz}$, $a_{\uparrow\downarrow}^{3D} = -1800 a_0$, and $a^{3D} = 1100 a_0$. In this manner, the weakly interacting regime is reached when the inequality $1/\ln(a_{\uparrow\downarrow}/a) = 0.05 \ll 1$ is satisfied. In addition, by applying the Bogoliubov theory and the diffusion Monte Carlo simulation for $n_0 a^2 = 5 \times 10^{-10}$, the requirement of dilute liquids $na^2 \ll 1$ around the equilibrium density $n_0 = 2.5 \times 10^{14} \text{ m}^{-2}$ is also satisfied. Accordingly, after the energy density E_{2D} including all allowed scattering paths is calculated, the liquid phase properties in free space can be obtained by minimizing the grand potential density at zero pressure.

III. THEORETICAL MODEL FOR ROTATING QUANTUM DROPLETS

Since it is much easier to analyze the motion of a rotating object in the noninertial reference frame, the following work will be conducted based on the rotating frame Hamiltonian H_r given by the unitary transformation, $H_r = H_l - \vec{\Omega} \cdot \vec{L}$, from the lab frame Hamiltonian H_l , where $\vec{\Omega}$ is the angular velocity and \vec{L} is the orbital angular momentum (OAM) of the object. In this manner, with the inclusion of the high-order quantum fluctuations on the condensed cold atoms, the LHY-amended time-dependent GPE for a symmetric anharmonically-trapped rotating QD can be written as

$$i\hbar \frac{\partial \Psi}{\partial t} = \frac{1}{2M} (-i\hbar \vec{\nabla} - M\Omega \hat{z} \times \vec{r})^2 \Psi + \left[\frac{1}{2} M(\omega_0^2 - \Omega^2) r^2 + \frac{1}{4} \lambda' r^4 \right] \Psi + \frac{8\pi\hbar^2}{M \ln^2(a_{\uparrow\downarrow}/a)} |\Psi|^2 \ln(|\Psi|^2/n_0) \Psi \quad (1)$$

in which ω_0 denotes the angular frequency of the harmonic trap, λ' denotes the strength parameter of the quartic potential energy. The first term on the right-hand side of Eq. (1) precisely shows that the rotating droplet moves as a charge q in the xy plane subjected to a synthesized magnetic field $B\hat{z}$ with a vector potential $(q/c)\vec{A} = M\Omega\hat{z} \times \vec{r}$, giving the cyclotron frequency $\Omega = qB/2Mc$. Setting the effective magnetic length equal to unity and

applying the Rodrigues definition of the associated Laguerre polynomial

$$L_\nu^k(t) = \frac{1}{\nu!} e^t t^{-k} \frac{d^\nu}{dt^\nu} (e^{-t} t^{\nu+k}), \quad (2)$$

the eigenfunctions of the system composed of non-interacting and harmonically-trapped particles can be derived as

$$\chi_{n_l, m}(\vec{r}) = \frac{1}{\sqrt{2\pi}} \sqrt{\frac{n_l!}{2^{|m|}(|m| + n_l)!}} r^{|m|} e^{-r^2/4} e^{im\phi} L_{n_l}^{|m|} \left(\frac{r^2}{2} \right), \quad (3)$$

where integers $n_l = 0, 1, 2, \dots$ denote the Landau level index and $m = 0, \pm 1, \pm 2, \dots$ corresponds to the degenerate states within a Landau level.

For low-dimensional uniform liquids, it is found that the typical length scale on which Ψ changes is in order of the healing length, and the surface tension is crucial to the finite size effects on the droplet's energy and surface mode spectrum. To generalize the investigation to nonuniform liquids, a strong confinement is imposed with the sum of quadratic and quartic components, which manages to compensate for the centrifugal repulsion and stabilize the deformed droplet under fast rotations. Moreover, as the centrifugal potential $-M\Omega^2 r^2/2$ becomes influential at rapid rotations, the combined trapping potential leads to an effective Mexican hat trap. The atomic liquid becomes similar to the complex Schrödinger field interacting with the electromagnetic field in the Higgs-type potential, where the magnetic flux is squeezed into quantized vortices, as is well-known in superconductors. This similarity may thus bring the topological relevance between vortex solitons and rotating droplets.

While the presence of the attractive inter-particle interactions would like to mix different (n_l, m) states, the LLL approach corresponding to $n_l = 0$ would be insufficient to describe the rotating droplets, especially for the strongly confined atoms, since the density will not be thinned out in the xy plane, as was observed in the vortex lattices that bear repulsive inter-particle interactions therein. Inspired by the work for a 2D Wigner crystal in a strong magnetic field [53], the ground state properties of the droplet matter waves in this work are examined using the variational method to minimize the energy functional $E[\Psi, \Psi^*]$ established in terms of the trial wavefunction

$$\Psi = C_m (\mathcal{Z} - \mathcal{Z}_0)^m \exp \left[-\frac{(\vec{r} - \vec{R})^2}{4\rho^2} - \frac{i}{2l_z^2} \hat{z} \cdot (\vec{r} \times \vec{R}) \right] \exp \left[i\frac{\alpha}{4} (\vec{r} - \vec{R})^2 \right] \exp \left[i\frac{\vec{p}}{2\hbar} \cdot (\vec{r} - \vec{R}) \right], \quad (4)$$

in which \mathcal{Z} and \mathcal{Z}_0 are the complex notations of the 2D position vectors, and by the moment the polar coordinates representation is taken, the azimuthal phase $\exp(im\phi)$ with an

integer number m embedded in $(\mathcal{Z} - \mathcal{Z}_0)^m$ introduces the quantum mechanical OAM of a rotating QD. Characterized in the length scale l_z , the parameter ρ sketches the width of the wavepacket and is representative of the influence of the LLM effect that should be addressed unless an extremely high magnetic field or rapid rotation is reached, where the assumption of the LLL with $\rho = 1$ will be feasible. While $\vec{r} = x\hat{x} + y\hat{y}$ is the position of the particle in the droplet and $\vec{R} = X_0\hat{x} + Y_0\hat{y}$ denotes its center-of-mass (CM) position, the inclusion of an additional phase associated with $\vec{r} \times \vec{R}$ leaves the possibility for rigid-body rotation, and ensures the Gauge invariance under the synthetic magnetic field. The parameters α and \vec{p} in the last two phase terms of Eq. (4) denote the conjugate curvature coefficient and momentum that represent the inherent MF expansion and the relative repulsion of the wavepacket, respectively, making it possible for further investigation of the variation of the density profiles and coherent properties in the time evolution of the QD. Since the conservation of the particle number is required in the absence of the dissipation due to three-body collisions, the wavefunction normalization gives $C_m = \sqrt{N2^{m+1}/\pi m!}/\rho^{m+1}$.

For convenience, we map the system onto a 2D complex plane by introducing the dimensionless complex coordinates $\mathcal{Z}_0 = \frac{1}{2}(X_0 + iY_0)$, $\mathcal{Z} = \frac{1}{2}(x + iy)$, and momentum $\mathcal{P} = \frac{1}{2}(p_x + ip_y)$, and then $|\mathcal{Z}_0|^2 = R^2/4$, $|\mathcal{Z}|^2 = r^2/4$, and $|\mathcal{P}|^2 = p^2/4$ settle the complex-real connections. In this manner, the wavefunction reconstructed as

$$\begin{aligned} \Psi = & C_m(\mathcal{Z} - \mathcal{Z}_0)^m \exp \left[-\frac{1}{\rho^2} |\mathcal{Z} - \mathcal{Z}_0|^2 \right] \exp [\mathcal{Z}^* \mathcal{Z}_0 - \mathcal{Z} \mathcal{Z}_0^*] \exp [i\alpha |\mathcal{Z} - \mathcal{Z}_0|^2] \\ & \times \exp [i\mathcal{P}^*(\mathcal{Z} - \mathcal{Z}_0) + i\mathcal{P}(\mathcal{Z}^* - \mathcal{Z}_0^*)], \end{aligned} \quad (5)$$

will be helpful for simplifying the remaining calculations. Using the transformation relations $\partial/\partial\mathcal{Z} = \partial/\partial x - i\partial/\partial y$ and $\partial/\partial\mathcal{Z}^* = \partial/\partial x + i\partial/\partial y$, we define the complex creation and annihilation operators $a = -i(\mathcal{Z} + \partial/\partial\mathcal{Z}^*)/\sqrt{2}$ and $a^\dagger = i(\mathcal{Z}^* - \partial/\partial\mathcal{Z})/\sqrt{2}$ such that the differential operators $D_x = \partial/\partial x + iy/2 = i(a + a^\dagger)/\sqrt{2}$ and $D_y = \partial/\partial y - ix/2 = i(a - a^\dagger)/\sqrt{2}$ can also be defined as well. With these complex variables, it is easy to rewrite the Hamiltonian and calculate the energy functional based on Eq. (5). The recovery of the kinetic energy operator $K = -(D_x^2 + D_y^2)$ to an effective number operator $2a^\dagger a + 1$ gives

$$\int \Psi^* K \Psi d\vec{r} = \frac{N(m+1)}{2} \left(\rho^2 + \frac{1}{\rho^2} + \alpha^2 \rho^2 \right) - mN + N|\mathcal{P}|^2. \quad (6)$$

Similarly, the evaluation of the effective trapping potential energy shows that

$$\begin{aligned} \int \Psi^* V_{eff} \Psi d\vec{r} = & N (\omega_0^2 - 1) \left(\frac{m+1}{2} \rho^2 + |\mathcal{Z}_0|^2 \right) \\ & + N \lambda' \left[\frac{1}{4} (m+2)(m+1) \rho^4 + |\mathcal{Z}_0|^4 + 2(m+1) \rho^2 |\mathcal{Z}_0|^2 \right], \end{aligned} \quad (7)$$

In calculating the total OAM carried by the droplet,

$$\int \Psi^* L_z \Psi d\vec{r} = [i(\mathcal{P}^* \mathcal{Z}_0 - \mathcal{Z}_0^* \mathcal{P}) + m + 2|\mathcal{Z}_0|^2] N, \quad (8)$$

we find that three different mechanisms are involved: the wavepacket repulsion dynamics, quantum phase imprinting, and the rigid-body revolution. Finally, through equilibrating the spatial attraction and repulsion, the interatomic energy term,

$$\begin{aligned} \int |\Psi|^4 \ln \left(\frac{|\Psi|^2}{\sqrt{e}} \right) d\vec{r} = & \frac{N^2}{\pi(m!)^2 2^{2m+2}} \frac{1}{\rho^2} \left[(2m)! \ln \left(\frac{|C_m|^2}{4^m \sqrt{e}} \right) - \frac{(m+1)!}{2} \right. \\ & \left. + m\Gamma'(2m+1) + (2m)(2m)! \ln \rho \right], \end{aligned} \quad (9)$$

where $\Gamma'(x)$ is the derivative of the Gamma function for a positive integer x , demonstrates the self-bound feature.

A. Density Profiles and Phase Portraits

To investigate the stationary properties of the rotating QD, the condensate is assumed to be stirred adiabatically to ensure reaching equilibrium at certain Ω via the re-thermalization processes. Therefore, the knowledge of the scale of physical parameters such as system temperature, particle number, energy, and time becomes relevant in preserving the stationary properties of the QDs and in determining their stability and coherence against external perturbations. While the chemical potential and the healing length can be approximately expressed by $\mu \sim -n\hbar^2/M \ln^2(a_{\uparrow\downarrow}/a)$ and $\xi \sim \hbar/\sqrt{M|\mu|}$, respectively, and the latter represents the vortex core size of the rotating QD as well, they are approximately -0.412 and 2.2 at $n = 1.1n_0$ on the dimensionless scales. Moreover, with the previously determined equilibrium density and the characteristic length, we obtain the particle number scale $\tilde{N} = n_0 l_z^2 = 81$. For the energy scale $\tilde{E} = \hbar\omega_z \sim 1.65 \text{ peV}$, the calculation of the ground state energy of this work shows that a rotating droplet of hundreds of atoms can

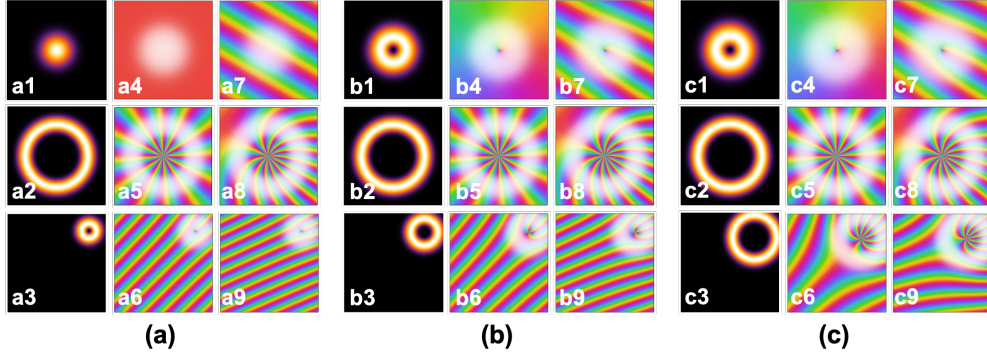


FIG. 1. (color online) Density profiles and phase portraits for (a) $N = 20$, (b) $N = 60$, and (c) $N = 100$, corresponding to $\Omega = 0.6, 1.4, 1.8$ (top to bottom) and initial momentum $p_x = 0, p_y = 0$ (middle), $p_x = \sqrt{2}, p_y = \sqrt{6}$ (right).

be stably sustained in the extremely low temperatures of approximately tens of Kelvin, indicating that the time scale for tracing the droplet's dynamics before collapse approaches $\tau = 1/\omega_z = 0.4$ ms.

Using these parameters, we reveal that by minimizing the energy functional constructed associated with Eqs. (6)-(9) with respect to ρ and R , the solutions of the coupled equations $\partial E/\partial \rho = 0$ and $\partial E/\partial R = 0$ would return the optimal information of the OAM quantum number m , wavepacket width ρ , and the CM position R of the ground state. After that, the influences of the confinement, nonlinear interaction, and rotational speed on the QD's ground state configuration can also be studied.

Figure 1 shows the density profiles and phase portraits for (a) $N = 20$, (b) $N = 60$, and (c) $N = 100$, corresponding to $\Omega = 0.6, 1.4, 1.8$ (top to bottom) and initial momentum $p_x = 0, p_y = 0$ (middle), $p_x = \sqrt{2}, p_y = \sqrt{6}$ (right). At slow rotations, it is found that when the particle number is low, the CM state with $m = 0$ and $R = 0$ is the energetically favorable ground state, even when Ω is slightly larger than 1, as shown in Fig. 1(a1). When the particle number increases, the repulsive LHY interaction plays a decisive role in the formation of the vortex states with nonzero m , such as the doughnuts shown in Figs. 1(b1) and (c1) that both correspond to $m = 1$. For these two states, the respective width of the wavepacket is $\rho = 1.3$ and $\rho = 1.4$, effectively showing the mixing of higher Landau levels.

As we increase the rotational speed to $\Omega = 1.4$, Figs. 1(a2), (b2), and (c2) show the possibility of the formation of giant vortices with $m \geq 10$ and large cores due to strong

centrifugal forces. Consequently, along with large surface tension generation in the presence of the peculiar nonlinear interaction between liquid atoms, the narrowing of the wavepacket to $\rho < 1$ starts to be evident. On the other hand, at even faster rotations with $\Omega = 1.8$, the system prefers to form off-centered vortex states with nonzero R instead, such as shown in Figs. 1(a3), (b3), and (c3). For these deflected QDs, the cores of the vortices enlarge with the increase in the particle number, but are lower than those of the aforementioned vortex states. Within weakly nonlinear interactions, this phenomenon can be attributed to the counterbalance between the centrifugal force and the strong compression provided by the anharmonic potential.

In the middle and right columns, the colored lines depict the spatial phase distribution for the QD subjected to a zero initial drive $\vec{p}(0) = 0$ and a finite drive $\vec{p}(0) \neq 0$, respectively. For the CM state without OAM, the phase portrait in (a4) shows that in the absence of an initial drive, the QD is static and has a spatially homogeneous phase distribution, whereas the plane wavefronts displayed in (a7) are the revelation of tendency of the wave propagation when suffering an instant linear drive. On the other hand, for vortex states and off-centered vortex states that carry nonzero OAM, the quantum number m or the topological charge number, is the repetition rate of phase variation in 2π that is visually depicted by the colored lines in the spatially nonhomogeneous phase distributions within the radial-like patterns [middle row: (a5) and (a8), (b5) and (b8), (c5) and (c8)] and the fork-like patterns [(b7), and the bottom row: (a6) and (a9), (b6) and (b9), (c6) and (c9)]. The launch of an instant linear drive produces strain on the surface of the QD that causes an additional phase imprinting upon its wavefunction. The linear phase carries nothing related to the rotation, and therefore modifies the slope of wavefronts only, but not the repetition rate of phase variation.

B. Analogy with Optical Vortices

To better interpret the underlying physics of the phase portraits, a brief comparison between the rotating QDs and the optical vortices is made since the two bosonic systems share a number of key features. In 1992, Allen et al. recognized that in addition to the spin angular momentum, light beams with an azimuthal phase dependence of $\exp(i\ell\phi)$ refer to a nonzero OAM, $\ell\hbar$, imposition on the photons [54]. The conception has been realized

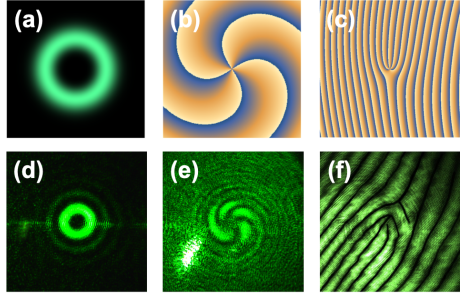


FIG. 2. (color online) The theoretical simulation (upper panel) and the experimental generation (lower panel) of the LG_{04} mode optical vortex with both intensity and phase singularities. In (b) and (e), the spiral phase distributions are the interference fringes of the optical vortex and a Gaussian spherical wave, whereas the interference fringes of the optical vortex and a Gaussian plane wave depict the fork-like phase distributions as shown in (c) and (f).

and extensively applied to optical trapping and manipulation, super spatial resolution microscopy, and material processing [55–57]. In the paraxial approximation, the solution of the Helmholtz equation of a cylindrical symmetric optical vortex measured at the beam waist ω_0 is the Laguerre-Gaussian function,

$$LG_{p\ell}(r, \phi, 0) = \sqrt{\frac{2p!}{\pi(p + |\ell|)!}} \frac{1}{\omega_0} \left[\frac{\sqrt{2}r}{\omega_0} \right]^{| \ell |} \exp[i\ell\phi] \exp\left[\frac{-r^2}{\omega_0^2}\right] L_p^{|\ell|}\left(\frac{2r^2}{\omega_0^2}\right), \quad (10)$$

where the radial index p of the number of nodes and the angular index ℓ are equivalent to the parameters of the Landau level index n_l and the degenerate states m within a Landau level in Eq. (3). Similarly, referring to Eq. (5), the role of the angular index ℓ is equivalent to the OAM quantum number m of the QD. Therefore, the optical vortex can be thought of as the classical correspondence of the rotating QD.

In Fig. 2, we demonstrate the theoretical simulation for (a) the density profile of the LG_{04} mode, and the phase distribution of the optical vortex extracted by performing the interference of the optical vortex with (b) a Gaussian spherical wave and (c) a Gaussian plane wave. Accordingly, by using the spatial light modulator, the experimental images captured by the first-order diffraction at the focal length are also displayed in (d)-(f). In these patterns, the discontinuity along the radial direction is the indication of the emergence of the intensity singularity, whereas the emergence of the phase singularity is identified when the discontinuity occurs along the azimuthal direction. In the optical system, it is clear that both the number of spiral blades and the number of dark bands in the fork-like interference

fringe symbolize the OAM quantum number, also termed the topological charge, of an optical vortex. Likewise, the same rules can be applied to the atomic system of QDs. As a result, the number of color bands split from the singular point of a vortex core displayed in the phase portraits of Fig. 1 can be claimed as the visual identification of the OAM carried by a QD. For example, in Fig. 1(c), where $N = 100$, we can now identify $m = 1$ for $\Omega = 0.6$, $m = 12$ for $\Omega = 1.4$, and $m = 8$ for $\Omega = 1.8$. To the best of our knowledge, there has been no research analysis on the phase distributions of the rotating QDs. Therefore, the analogy with optical vortices provided in this work has suggested the rules for further experimental verification of the OAM carried by the QDs, thus inspiring a challenging interferometer architecture for the precise measurement of the singular and the coherent properties of the rotating QDs with adjustable two-species nonlinear interactions.

C. Phase Diagram

As the term $-\Omega L_z$ characterizes the Hamiltonian of a rotating QD, it is intuitively that the vortex state with highly quantized circulation is energetic favorable. The plot of energy variation as a function of Ω in Fig. 3(a) confirms this tendency. With the increase of Ω , the phase transition from the CM state with $m = 0$ to the vortex states with multiple quantized circulations such as $m = 1, 3, 5, \dots, 11$ and lower energies takes place to maintain the QD's stability. Correspondingly, the expectation value of a single particle's total OAM $\langle L_z \rangle = m + 2|Z_0|^2$ will increase sharply and endlessly with the increase of Ω , as the red curve shows in Fig. 3(b). However, it should be addressed that to maintain bounded QDs at extremely high rotational speed, the emergence of strong attractions between the squeezed atoms inside the thin rings becomes inevitable in the fast expansion of the core size due to the very large quantum phase imprinting on the vortex states. As a result, the QDs may teeter on the edge of collapse in the presence of the three-body collisions. To avoid such a collapse and the numerical divergence, we suggest restricting the maximum of the quantized circulation m of the vortex state in the energy minimization by applying the LLL approximation with $\rho = 1$, since this approach is valid in the rapid rotation regimes. With this simplification, the upper bound of the circulation $m_{\max} = (\Omega_c - \epsilon/2 - 1)/\lambda' - 1$, in which $\epsilon = \omega_0^2 - 1$, can be estimated for a given cutoff Ω_c . In this work, $\Omega_c = 2$ is taken as the high rotational speed threshold, beyond which all the cold atoms in the QD are expected to

collapse to the LLL and form a macroscopic coherent population. Therefore, for $\omega_0 = 0.5$ and $\lambda' = 0.1$, the calculation for determining the ground state configuration is limited in the range below $m_{\max} = 12$. Due to this restriction, the allocation of the total OAM between the quantum part and the classical part can occur. Instead of forming a vulnerable giant vortex QD with huge circulation, the formation of an off-centered vortex QD with a moderate circulation and deflected CM position of $R = 2\sqrt{\Omega - \epsilon/2 - 1 - (m+1)\lambda'\rho^2}/\sqrt{\lambda'}$ at certain rotational frequency may become more energetically favorable. Accordingly, the limiting fraction of the cross-sectional area occupied by the vortex cores estimated in the Thomas-Fermi regime for dilute atomic gases [58] can also be validly applied for QDs.

The consequences of our statement for determining a proper ground state are visualized in Figs. 3(b) and (c). While considering the restriction of maximum circulation, the red curve of a monochromatic increasing total OAM is replaced with the zonal increasing blue curve, in which an extended plateau specifying m_{\max} of $\langle L_z \rangle$ between Ω_1 and Ω_2 appears. For $\Omega < \Omega_1$, the vortex states in the gray region (b1) with $m < m_{\max}$, for example, the (c1) state with $m = 1$ at $\Omega = 0.6$, are energetically favored stable states. For $\Omega > \Omega_1$, the pink region (b2) that contains unstable vortices carrying huge circulation quanta and vortex cores such as the vortex in (c2) shows, where $m = 53$ at $\Omega = 1.8$, no longer holds. Instead, the vortex states with bounded $m = m_{\max} = 12$, such as (c3) shows, will occupy the plateau (b3), and for $\Omega > \Omega_2$, the off-centered vortex states such as the one shown in (c4), where $m = 3$, $R = 6.11$ at $\Omega = 1.8$, are rather stable and will dominate the extremely rapid rotating regimes (b4).

After the sectional view of how the ground state profiles at a fixed N change with the increase of the rotation speed, the influences of the maximum circulation restriction on the ground state of the system with different particle number is further explored. The N - Ω phase diagram demonstrated in Fig. 3(d) is divided into four regions, in which (i) depicts the region corresponding to the unstable CM state, (ii) the vortex state, (iii) the off-centered vortex state, and (iv) the off-center-of-mass (OCM) state. Across the boundary of (ii) and (iii), the phase transition from the vortex state to the off-centered vortex state occurs. The QDs attempt to keep stable at extremely high rotational speed Ω by abruptly lowering their rotational inertia concerning the CM of the atoms via shrinking the vortex core size but raising the rotational kinetic energy via configuring themselves to off-centered vortices. Otherwise, the formation of vortex states with huge cores far beyond the theoretical limit

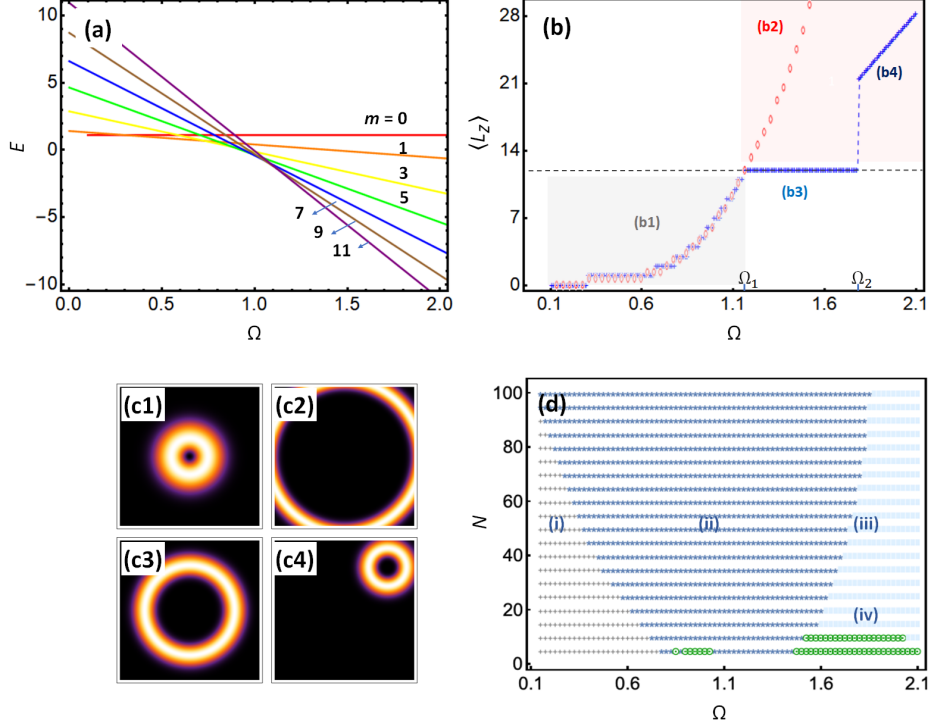


FIG. 3. (color online) For $N = 60$, (a) shows the plot of the energy variation as a function of Ω for the CM state with $m = 0$ and certain vortex states corresponding to $m = 1, 3, \dots, 11$. (b) The blue and red curves show the expectation value of the total OAM $\langle L_z \rangle$ as a function of Ω with and without following the restriction of maximum circulation, which enables the presence of an extended plateau between Ω_1 and Ω_2 that specifies the vortex states with $m = m_{\max}$ and the presence of the stable off-centered vortex states in the extremely rapid rotation regimes. (c1)-(c4) depict the density profiles of the QD corresponding to (b1)-(b4) region, respectively. (d) The N - Ω phase diagram, in which (i) depicts the region corresponding to the center-of-mass state, (ii) the vortex state, (iii) the off-centered vortex state, and (iv) the off-center-of-mass state.

and squeezed atomic distribution, such as the density profile shown in (c2), would effectively have an inter-attractive interaction, and thus is only metastable and fragile against three-body collisions. In addition to the formation of energetically favored off-centered vortex states in region (iii), we found that there can be some OCM states embedded in the few particle and fast rotation regimes (iv).

When the particle number is low, the QDs of ultra-dilute liquids can be stably sustained if they are energetically more favorable than the atomic cloud subjected to an effective 2D

MF interaction given by

$$V^{2D}(\vec{r}) = \frac{\sqrt{8\pi}\hbar^2 a_s}{ml_z} \delta^{2D}(\vec{r}). \quad (11)$$

Thus we found that the presence of OCM states approaching $\Omega = 1$ in Fig. 3(d) is the signature of the dynamic instability that the gas-liquid phase transition can be induced due to particle fluctuations.

It should be noted that for certain N and Ω , the stability condition

$$\frac{\partial^2 E}{\partial \rho^2} \frac{\partial^2 E}{\partial R^2} - \left(\frac{\partial^2 E}{\partial \rho \partial R} \right)^2 > 0 \quad (12)$$

must be satisfied when determining the QD's ground state. Therefore, while the CM states in the region (i) are found to violate the inequality, the system would try to maintain its stability by removing the atoms from the dense peak to pinning on the trap center, resulting in the creation of the embedded vortex with multiple circulations when initiating a rotation. Although it was reported that the multiple singly quantized vortex clusters can be created in the QDs at slow rotations [59], they are metastable and cause the deformation of the QDs.

IV. DYNAMICS OF ROTATING QUANTUM DROPLETS

To investigate the QD's dynamics and configuration stability, we employ Hamilton's principle of least action

$$\delta S[\Psi^*, \Psi] = \int dt \int d\vec{r} \delta \mathcal{L}(\Psi, \Psi^*, \dots) = 0, \quad (13)$$

based on the stationary condition for any Lagrangian density \mathcal{L} constructed in terms of the wavefunction, its complex conjugate, and their derivatives given by

$$\mathcal{L} = \frac{i\hbar}{2} \left(\Psi^* \frac{\partial}{\partial t} \Psi - \Psi \frac{\partial}{\partial t} \Psi^* \right) - \Psi^* H \Psi. \quad (14)$$

Using Eq. (5), the spatial integration of the Lagrangian density involving the time derivative terms gives

$$\int \frac{i}{2} \left(\Psi^* \frac{\partial \Psi}{\partial t} - \Psi \frac{\partial \Psi^*}{\partial t} \right) d\vec{r} = -iN(\mathcal{Z}^* \dot{\mathcal{Z}}_0 - \mathcal{Z} \dot{\mathcal{Z}}_0^*) - \frac{N}{2}(m+1)\dot{\rho}^2 + N(\mathcal{P}^* \dot{\mathcal{Z}}_0 + \mathcal{P} \dot{\mathcal{Z}}_0^*). \quad (15)$$

Along with the calculation results in Eqs. (6)-(9), the derivation of the Lagrange function per atom leads to:

$$\begin{aligned}
\mathfrak{L} = & -i(\mathcal{Z}^* \dot{\mathcal{Z}}_0 - \mathcal{Z} \dot{\mathcal{Z}}_0^*) - \frac{1}{2}(m+1)\dot{\alpha}\rho^2 + (\mathcal{P}^* \dot{\mathcal{Z}}_0 + \mathcal{P} \dot{\mathcal{Z}}_0^*) - \frac{m+1}{2} \left(\frac{1}{\rho^2} + \alpha^2 \rho^2 \right) \\
& - \omega_0^2 \left(\frac{m+1}{2} \rho^2 + |\mathcal{Z}_0|^2 \right) - \lambda \left[\frac{1}{4}(m+2)(m+1)\rho^4 + |\mathcal{Z}_0|^4 + 2(m+1)\rho^2 |\mathcal{Z}_0|^2 \right] \\
& - \frac{N}{\pi(m!)^2 2^{2m+2}} \frac{1}{\rho^2} \left[(2m)! \ln \left(\frac{|C_m|^2}{4^m \sqrt{e}} \right) - \frac{(m+1)!}{2} + m\Gamma'(2m+1) + (2m)(2m)! \ln \rho \right] \\
& + \Omega [i(\mathcal{P}^* \mathcal{Z}_0 - \mathcal{Z}_0^* \mathcal{P}) + m+2|\mathcal{Z}_0|^2] - i(\mathcal{P}^* \mathcal{Z}_0 - \mathcal{Z}_0^* \mathcal{P}) - (|\mathcal{Z}_0|^2 + |\mathcal{P}|^2), \tag{16}
\end{aligned}$$

through which the Euler-Lagrange equations and the equations of motion of the corresponding characteristic parameters can be obtained, i.e.,

$$\frac{d}{dt} \left(\frac{\partial L}{\partial \dot{\mathcal{P}}^*} \right) - \frac{\partial L}{\partial \mathcal{P}^*} = 0 \quad \text{gives} \quad \dot{\mathcal{Z}}_0 = \mathcal{P} - i(\Omega - 1). \tag{17}$$

$$\begin{aligned}
\frac{d}{dt} \left(\frac{\partial L}{\partial \dot{\mathcal{Z}}_0^*} \right) - \frac{\partial L}{\partial \mathcal{Z}_0^*} = 0 \quad \text{gives} \quad \dot{\mathcal{P}} = & -2i\dot{\mathcal{Z}}_0 - (\omega_0^2 - 1) \mathcal{Z}_0 - 2\lambda |\mathcal{Z}_0|^2 \mathcal{Z}_0 \\
& - (\Omega - 1) \mathcal{P} + 2\mathcal{Z}_0 (\Omega - 1) - 2(m+1)\lambda \rho^2. \tag{18}
\end{aligned}$$

$$\frac{d}{dt} \left(\frac{\partial L}{\partial \dot{\alpha}} \right) - \frac{\partial L}{\partial \alpha} = 0 \quad \text{gives} \quad \dot{\rho} = \alpha \rho. \tag{19}$$

$$\frac{d}{dt} \left(\frac{\partial L}{\partial \dot{\rho}} \right) - \frac{\partial L}{\partial \rho} = 0 \quad \text{gives} \quad \dot{\alpha} = -\frac{1}{N(m+1)\rho} \frac{\partial E}{\partial \rho}. \tag{20}$$

A. Periodicity and Stability

Based on Eqs. (17)-(20), we are able to trace the QD's dynamics by solving multiply-coupled complex equations for the characteristic parameters $\rho, \alpha, \mathcal{Z}_0$, and \mathcal{P} under an external drive $\vec{p}(t)$ with the initial values $p_x(0) = \sqrt{2}$ and $p_y(0) = \sqrt{6}$. Since the particle number is found to be qualitatively irrelevant to the simulation results, we choose $N = 20$ for general cases study and $N = 100$ for a special case study. In Fig. (4), the orange circles on the green and brown curves depict the initial CM position and the conjugate momentum of the unperturbed QDs, and the orange triangles denote the corresponding parameters of the perturbed QDs at some moment after the long-term evolution.

Because of the lack of rotational kinetic energy, Fig. 4(a1) and (a2) show that after an initial kick, the QD moves as if it were circulating in a cyclotron oscillator and accelerated by an effective AC voltage produced by Eq. (18) that involves especially the positive contribution from $-(\Omega - 1)\mathcal{P}$ for $\Omega = 0.6$. As a result, both the rapid decrease in the wavepacket

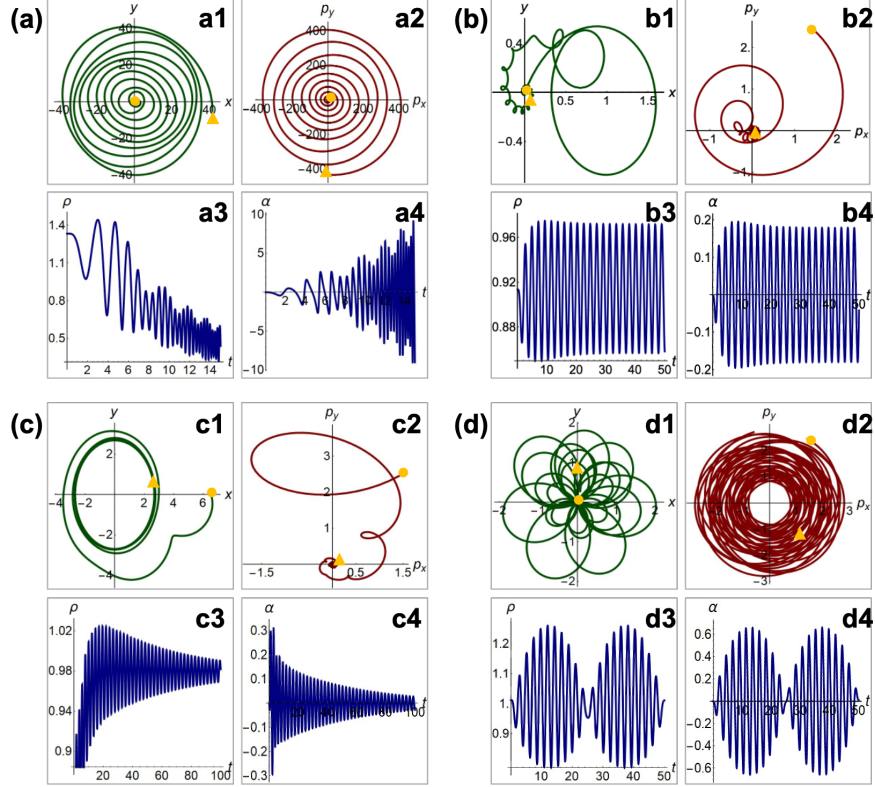


FIG. 4. (color online) Trajectory diagrams of \vec{R} and \vec{P} , and time variation of width ρ and conjugate curvature coefficient α under an external drive $\vec{p}(t)$ with the initial values $p_x(0) = \sqrt{2}$ and $p_y(0) = \sqrt{6}$ for (a)-(c) $N = 20$ and $\Omega = 0.6, 1.4$, and 1.8 , (d) $N = 100$ and $\Omega = 1.0$. The orange circles on the green and brown curves depict the initial CM position and the conjugate momentum of the unperturbed QDs, and the orange triangles denote the corresponding parameters of the perturbed QDs at some moment after the long-term evolution.

width and increase in the curvature in Fig. 4(a3) and (a4) are the manifestation of the state instability as it has been recognized. Eventually, the QD of the CM state configuration would crash when it escapes from the trap confinement.

With the increase in rotational speed, for example $\Omega = 1.4$, the drift of a vortex state QD after the initial kick of a linear force breaks the axial symmetry, thus exciting the system to a high energy state. In contrast to the slow rotation case (a), due to the negative contribution $-(\Omega - 1)\mathcal{P}$, Eq. (18) may play the role of the restoring force that pulls the QD to the equilibrium point, i.e., the trap center, as Figs. 4(b1) and (b2) show. At the same time, it is clearly shown in (b3) and (b4) that the energetically favored vortex state would like to verify that it can be stably sustained under a long-term evolution by regularly adjusting the

ring size to keep a sufficient surface tension via the LLM effect.

At extremely rapid rotations, for example $\Omega = 1.8$, Fig. 4(c1) and (c2) show that the attempts of a QD of the off-centered vortex state to maintain the dynamic stability are displayed by lowering the quantum mechanical OAM $m\hbar$ and shrinking itself to steadily precess around the trap center. In this case, when the steady state of the system is reached after the long-term evolution, the approaching of $\rho = 1$ in the wavepacket width (c3) and zero variation of the conjugate curvature of the QD provide strong support for the validity of LLL approximation suggested in this work.

It is interesting to analyze a special case where $\Omega = 1.0$. At this speed of rotation, the externally-applied effective centripetal force for an orbital motion vanishes, leaving a nonzero Coriolis force induced by the velocity variation in the zonal direction that launches a self-curing rotational motion for the QD. As shown in Fig. 4(d), the quasi-periodic trajectories [(d1) and (d2)] and breathings [(d3) and (d4)] provide evidence of the emergence of the collective excitation of the surface mode in the vortex state. In the presence of the anharmonic trapping and the nonlinear effects, the orbit of the QD does not strictly close upon itself after a finite number of oscillations, and neither does it open. Instead, as the lobes reveal, the evolution of the QD shows a multiple-periodic motion between the turning points. Similar to that for a periodic motion driven by the central-force field, the area enclosed by the moving trajectory is still a rational fraction $2\pi(a/b)$ —after b periods, the radius of the vector of the QD will have made a complete revolutions and will have returned to its original position.

Different from this study, while the vortices for strongly interacting cases are much smaller than the system size and the radius of curvature of the density profile, the approaches for the homogeneous systems can be applied to support the formation of vortex arrays [25]. As a result, for a fixed OAM, the wave functions would be constructed in terms of the sum of noninteracting particle states of different angular momenta rather than the form of a macroscopic order parameter, as Eq. (4) presents. In contrast, in the region containing multiple quantized vortices, the vortex cores are large and the vortex density is suppressed such that the individual vortices become indiscernible [26]. Within harmonic confinement, a recent simulation based on imaginary-time evolution and variational method reported that, contrary to the repulsive Bose gases, a self-bound and visible triangular vortex lattice can be formed without melting for a rotating QD in the quantum Hall limit [34]. Moreover,

the analytic solution of the LHY-amended GPE based on a Gaussian trial wavefunction adopted in Ref. [33] shows the possibility of the formation of the vortex lattices in a tightly confined rotating BEC that bears total repulsive nonlinear interactions. Therefore, these studies reveal the requirements for the interatomic attraction and the counterbalance between nonlinear interactions, whenever the QDs with multiply quantized circulations are expected to be established. Accordingly, although the multiple quantized vortices carrying high topological charges are not thermodynamically stable and energetically favorable in the homogeneous superfluids or harmonic-confined systems, the periodicity and stability analyses in this work demonstrate that the vortex configurations in anharmonically-trapped rotating QDs can be stably supported.

B. Probability Current Density Distribution

Rotation at angular velocity $\vec{\Omega}$ can be regarded as a perturbation to the nonrotating Hamiltonian and can be interpreted via:

$$-\vec{\Omega} \cdot \vec{L} = -m \sum_{\mathbf{q}} \vec{j}_{\mathbf{q}}^{\dagger} \cdot \vec{A}_{\mathbf{q}}, \quad (21)$$

where $\vec{j}_{\mathbf{q}}^{\dagger}$ is the particle current density fluctuation and $\vec{A}_{\mathbf{q}}$ is the Fourier transform of the transverse artificial vector potential. With the application of linear response theory, this fluctuation will give rise to the mass current in the condensate frame. For low-energy scattering around $\mathbf{q} = 0$, the current density in the presence of the rotating field can be described by,

$$\vec{j} = \frac{\hbar}{2Mi} \left[\psi^*(\vec{r}) \vec{\nabla} \psi(\vec{r}) - \psi(\vec{r}) \vec{\nabla} \psi^*(\vec{r}) \right] - r\Omega |\psi(\vec{r})|^2 \hat{\phi}. \quad (22)$$

The substitution of a general condensate wavefunction $\psi(\vec{r}) = f(\vec{r})e^{i\phi(\vec{r})}$ in Eq. (22) gives $\vec{j} = (\hbar/M) \vec{\nabla} \phi(\vec{r}) |\psi(\vec{r})|^2 - r\Omega |\psi(\vec{r})|^2 \hat{\phi}$, and the corresponding velocity field $\vec{v} = (\hbar/M) \vec{\nabla} \phi(\vec{r}) - r\Omega \hat{\phi}$. Therefore, a rotational potential flow can be generated in the QDs with quantized circulation if there are singularities in the local phase $\phi(\vec{r})$. Different from the field-free system, the current density distribution is adjusted by the field-induced effective dipole revolution about the rotation axis.

On the basis of Eq. (5), the dimensionless total current density of the QD consists of four

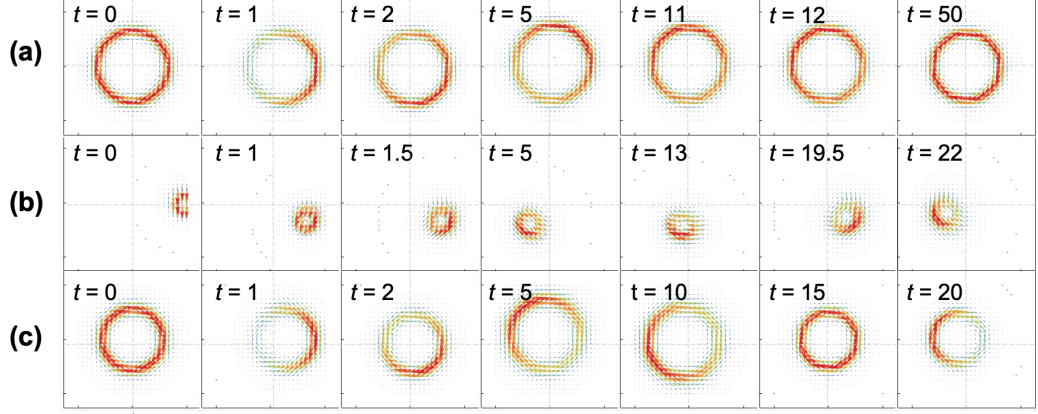


FIG. 5. (color online) Snapshots of the rotation field adjusted current density distribution taken for a long-term evolutionary quantum state referring to Fig. 4, corresponding to (a) $N = 20$ and $\Omega = 1.4$, (b) $N = 20$ and $\Omega = 1.8$, and (c) $N = 100$ and $\Omega = 1.0$.

parts:

$$\begin{aligned} \vec{j} = & \frac{1}{2} g_m(\vec{r}, \vec{R}) \left\{ 4m(\vec{r} - \vec{R})^{-2} \left[-(y - Y_0) \hat{x} + (x - X_0) \hat{y} \right] + \alpha \left[(x - X_0) \hat{x} - (y - Y_0) \hat{y} \right] \right. \\ & \left. + (p_x \hat{x} - p_y \hat{y}) + (2\Omega y - Y_0) \hat{x} + (X_0 - 2\Omega x) \hat{y} \right\}, \end{aligned} \quad (23)$$

in which $g_m(\vec{r}, \vec{R}) = 4^{-m} C_m^2 (\vec{r} - \vec{R})^{2m} \exp \left[-(\vec{r} - \vec{R})^2 / 2\rho^2 \right]$. As expected, the superfluid annular flow can be observed in the quantum states with nonzero circulation quanta. For vortex states, the atomic flow can be steadily circulating around the vortex core if no external drives act upon the QDs. In contrast, the deflection of the CM position of the off-centered vortex states breaks the rotational symmetry of the system and acquires a classical rigid body-like OAM that boosts the variation of the circulating flow.

In Fig. 5, we demonstrate a series of snapshots of the current density distribution taken for a long-term evolutionary quantum state referring to Fig. 4, corresponding to (a) $N = 20$ and $\Omega = 1.4$, (b) $N = 20$ and $\Omega = 1.8$, and (c) $N = 100$ and $\Omega = 1.0$. It is interesting to find that the presence of the rotating field reverses the circulation direction that is observed to be counterclockwise in the field-free case. The reversal caused by this correction shown in Eq. (22) is thus manifesting the guidance of the stirring laser field that governs both the static and the dynamic properties of the QDs. Another interesting feature is that, different from the atomic gas system of the mixtures, the counterbalance against the strong centrifugal force due to high-speed rotation can be reached thanks to the coexistence of the repulsive-

attractive nonlinear interaction, which establishes a strong but flexible surface tension and keeps the QDs away from being deformed in the long-term rapid rotating evolution.

From Fig. 5(a), (b), and (c), it is clear that the successive expansion and contraction of the ring give the QD a fresh impetus to the next movement. Confined in a quadratic plus weak quartic trapping potential, the variation in the ring size is also a direct reflection of a quasi-harmonic oscillation. Therefore, driven by an initial impulse at $t = 0$, the spatially homogeneous current density distributions imply that the QD is about passing through the equilibrium point. At the moment the QD has a larger ring size, it approaches the end point. As the mechanical energy conservation is obeyed, the nonlinear restoring force would manage to regulate the QD into a stable revolution. Under the rotating field, the imbalance in the current field distributions at $t > 0$ depicts the direction of the centrifugal force, thus precisely locating the QD of the off-centered vortex state such as shown in (b). As a contrast, the reappearance of spatially homogeneous current distributions in the vortex states is a signature of the approach of the dynamic equilibrium of the system, which can be the stationary state such as at $t = 50$ in (a), or the equilibrium point of the oscillation such as at $t = 15$ in (c). Different from the studies of superfluidity including the observation of persistent flows conventionally performed in the ring traps [60–62], our dynamical analysis demonstrated that as the quantized vortex appears within the rotating field, the superfluid annual flow can be stably sustained by its angular momentum [63]. The multiply quantized vortex states obtained from Eq. (5) thus provide reliable initial states for further exploring the vortex dynamics and the flow persistency in the time-of-flight simulation.

In the experiments of vortex creation for the two-component dilute BEC gases [19], where the self-interaction of one component is different from the other, the Hamiltonian is assumed to be invariant under simultaneous rotation of all the hyperfine states. In that work, annular superfluids are generated due to a lack of a common kind of topological stability as a single-component system such as He-4. The reasoning, however, will not be applied to generating asymmetric superfluids in this work, since the scattering strength imbalance among different species has already been considered in the effective LHY nonlinear interaction, and therefore there is no spin current generation in this work.

V. CONCLUSION

This work has investigated the stationary properties and the dynamics of a rotating QD confined in a two-dimensional symmetric anharmonic trap. Based on the variational method, we analytically solved the LHY-amended GPE utilizing a trial wavefunction inspired by the work for a 2D Wigner crystal in a strong magnetic field, and have addressed the role of the LLM effect. As the Coriolis force experienced by the droplets in the rotating frame appears equivalent to the Lorenz force on a charged particle, our study has demonstrated that the artificial Lorenz forces can also be engineered for the new type of quantum liquid. Via controlling the nonlinear interaction and the rotation speed, the QD with embedded vortex having multiple quanta of circulation can be generated. For even higher rotation speed, the off-centered vortex states turn out to be energetically favorable. It was also found that the rigid-body-like OCM state can be formed in the few particle regimes. By depicting the $N - \Omega$ phase diagram, the route for the quantum phase transition was revealed, meaning that the manipulation of the intensity and phase singularities embedded in the rotating QDs and the exploration of the singularity-related novel phenomena in the kind of systems is feasible.

To better interpret the underlying physics of the phase singularities, a brief comparison of the rotating QD and the optical vortex was made. We found that the number of spiral blades and the number of dark bands in the fork-like interference fringes can be claimed as the visual identification of the OAM carried by a QD. To the best of our knowledge, there has been no research analysis on the phase distributions of the rotating QDs. Therefore, the rules suggested in this work have inspired a challenging interferometer architecture for the precise measurement of the singular and the coherent properties of the rotating QDs with adjustable two-species nonlinear interactions.

Further investigation of the long-term evolution of the rotating QDs allowed us to confirm the stability of the quantum states. With the application of the Hamiltonian principle and the Lagrange dynamics, we solved the multiply-coupled complex equations of motion to analyze the periodicity and stability of QD's breathing and trajectory. For a special case with $\Omega = 1$, we found that the vanishing of the externally-applied effective centripetal force for an orbital motion leaves a nonzero Coriolis force induced by the velocity variation in the zonal direction that launches a self-curing rotational motion. The quasi-periodic trajectories and breathings thus provide evidence of the emergence of the collective excitation of the

surface mode in the vortex state.

From the snapshots of the rotation field adjusted current density distribution taken for different quantum states, we found that the counterbalance against the strong centrifugal force due to high-speed rotation can be reached thanks to the coexistence of the repulsive-attractive nonlinear interaction, which establishes a strong but flexible surface tension and keeps the QDs away from being deformed in the long-term rapid rotating evolution. The combined nonlinear interaction and the anharmonic trapping potential provide the restoring force that guides the QD to a regular and stable revolution until the dynamic equilibrium is eventually reached.

Sharing many similarities between the quantum Hall system and the rotating BECs, the application of the same mathematical formalism in this work has proved that the QD with quantized circulation or multiply topological charges can be stably supported in anharmonic confinement. Our studies have shown the possibility to simulate the quantum Hall-type effects in a controlled manner with low-dimensional nonuniform quantum liquids. The systems of rotating BECs with multiple degrees of freedom of tunable parameters are versatile and can be promising for topological quantum computations.

VI. ACKNOWLEDGEMENT

We thank the Ministry of Science and Technology, Taiwan for partial financial support under grants NSTC 110-2221-E-845-004, NSTC 112-2622-E-845-001 and NSTC 112-2112-M-034-001. W. H. K. gratefully acknowledges Prof. Wen-Feng Hsieh for the helpful discussion.

-
- [1] M. H. Anderson, J. R. Ensher, M. R. Matthews, C. E. Wieman, and E. A. Cornell, *Science* **269**, 198 (1995).
 - [2] C. C. Bradley, C. A. Sackett, J. J. Tollett, and R. G. Hulet, *Phys. Rev. Lett.* **75**, 1687 (1995).
 - [3] K. B. Davis, M.-O. Mewes, M. R. Andrews, N. J. van Druten, D. S. Durfee, D. M. Kurn, and W. Ketterle, *Phys. Rev. Lett.* **75**, 3969 (1995).
 - [4] C. A. Regal, M. Greiner, and D. S. Jin, *Phys. Rev. Lett.* **92**, 040403 (2004).
 - [5] M. W. Zwierlein, C. A. Stan, C. H. Schunck, S. M. F. Raupach, A. J. Kerman, and W. Ketterle, *Phys. Rev. Lett.* **92**, 120403 (2004).

- [6] G. B. Partridge, K. E. Strecker, R. I. Kamar, M. W. Jack, and R. G. Hulet, Phys. Rev. Lett. **95**, 020404 (2005).
- [7] D. M. Eagles, Phys. Rev. **186**, 456 (1969).
- [8] T. Köhler, K. Góral, and P. S. Julienne Rev. Mod. Phys. **78**, 1311 (2006).
- [9] T. D. Lee, K. Huang, and C. N. Yang, Phys. Rev. **116**, 1135 (1957).
- [10] C. R. Cabrera, L. Tanzi, J. Sanz, B. Naylor, P. Thomas, P. Cheiney, and L. Tarruell, Science **359**, 301 (2018).
- [11] P. Cheiney, C. R. Cabrera, J. Sanz, B. Naylor, L. Tanzi, and L. Tarruell, Phys. Rev. Lett. **120**, 135301 (2018).
- [12] G. Semeghini, G. Ferioli, L. Masi, C. Mazzinghi, L. Wolswijk, F. Minardi, M. Modugno, G. Modugno, M. Inguscio, and M. Fattori, Phys. Rev. Lett. **120**, 235301 (2018).
- [13] I. Ferrier-Barbut, H. Kadau, M. Schmitt, M. Wenzel, and T. Pfau Phys. Rev. Lett. **116**, 215301 (2016).
- [14] M. Schmitt, M. Wenzel, F. Böttcher, I. Ferrier-Barbut, and T. Pfau, Nature **539**, 259 (2016).
- [15] I. Ferrier-Barbut, M. Wenzel, F. Böttcher, T. Langen, M. Isoard, S. Stringari, and T. Pfau, Phys. Rev. Lett. **120**, 160402 (2018).
- [16] L. Chomaz, S. Baier, D. Petter, M. J. Mark, F. Wächtler, L. Santos, and F. Ferlaino, Phys. Rev. X **6**, 041039 (2016).
- [17] D. S. Petrov, Phys. Rev. Lett. **115**, 155302 (2015).
- [18] Z. H. Luo, W. Pang, Y. Y. Li, and B. A. Malomed, Front. Phys. **16**, 32201 (2021).
- [19] M. R. Matthews, B. P. Anderson, P. C. Haljan, D. S. Hall, C. E. Wieman, and E. A. Cornell, Phys. Rev. Lett. **83**, 2498 (1999).
- [20] K. W. Madison, F. Chevy, W. Wohlleben, and J. Dalibard, Phys. Rev. Lett. **84**, 806 (2000).
- [21] B. P. Anderson, P. C. Haljan, C. A. Regal, D. L. Feder, L. A. Collins, C. W. Clark, and E. A. Cornell, Phys. Rev. Lett. **86**, 2926 (2001).
- [22] Z. Dutton, M. Budde, C. Slowe, and L. V. Hau, Science **293**, 663 (2001).
- [23] K. W. Madison, F. Chevy, V. Bretin, and J. Dalibard, Phys. Rev. Lett. **86**, 4443 (2001).
- [24] J. R. Abo-Shaeer, C. Raman, J.M. Vogels, and W. Ketterle, Science **292**, 476 (2001).
- [25] E. Lundh, Multiply quantized vortices in trapped Bose-Einstein condensates, Phys. Rev. A **65**, 043604 (2002).

- [26] P. Engels, I. Coddington, P. C. Haljan, V. Schweikhard, and E. A. Cornell, Phys. Rev. Lett. **90**, 170405 (2003).
- [27] A. Cidrim, F. E. A. dos Santos, E. A. L. Henn, and T. Macrì, Phys. Rev. A **98**, 023618 (2018).
- [28] B. A. Malomed, Physica D **399**, 108 (2019).
- [29] Y. Y. Li, Z. P. Chen, Z. H. Luo, C. Q. Huang, H. S. Tan, W. Pang, and B. A. Malomed, Phys. Rev. A **98**, 063602 (2018).
- [30] Y. V. Kartashov, B. A. Malomed, L. Tarruell, and L. Torner, Phys. Rev. A **98**, 013612 (2018).
- [31] J. Yang and Z. H. Musslimani, Opt. Lett. **28**, 2094 (2003).
- [32] Y. Y. Zheng, S. T. Chen, Z. P. Huang, S. X. Dai, B. Liu, Y. Y. Li, and S. R. Wang, Front. Phys. **16**, 22501 (2021).
- [33] R. T. Thiruvalluvara, S. Sabari, K. Porseziana, and P. Muruganandam, Physica E **107**, 54 (2019).
- [34] Q. Gu and X. L. Cui, arXiv preprint arXiv:2306.14958 (2023).
- [35] K. von Klitzing, G. Dorda, and M. Pepper, Phys. Rev. Lett. **45**, 494(1980).
- [36] K. von Klitzing, Rev. Mod. Phys. **58**, 519 (1986).
- [37] H. L. Stormer, Rev. Mod. Phys. **71**, 875 (1999).
- [38] D. C. Tsui, H. L. Stormer, and A. C. Gossard, Phys. Rev. Lett. **48**, 1559 (1982).
- [39] D. C. Tsui, Rev. Mod. Phys. **71**, 891 (1999).
- [40] N. R. Cooper and N. K. Wilkin, Phys. Rev. B **60**, R16279 (1999).
- [41] R. B. Laughlin, Phys. Rev. Lett. **50**, 1395 (1983).
- [42] J. K. Jain, *Composite Fermions*, Cambridge University Press, Cambridge (2007).
- [43] G. Moore and N. Read, Nucl. Phys. B **360**, 362 (1991).
- [44] N. Read and E. Rezayi, Phys. Rev. B **59**, 8084 (1999).
- [45] J. W. Reijnders, F. J. M. van Lankvelt, K. Schoutens, and N. Read, Phys. Rev. Lett. **89**, 120401 (2002).
- [46] R. J. Fletcher, A. Shaffer, C. C. Wilson, P. B. Patel, Z. Yan, V. Crepel, B. Mukherjee, and M. W. Zwierlein, Science **372**, 1318 (2022).
- [47] B. Mukherjee, A. Shaffer, P. B. Patel, Z. Yan, C. C. Wilson, V. Crepel, R. J. Fletcher, and M. W. Zwierlein, Nature **601**, 58 (2022).
- [48] C. Nayak, S. H. Simon, A. Stern, M. Freedman, and S. Das Sarma, Rev. Mod. Phys. **80**, 1083 (2008).

- [49] T. G. Skov, M. G. Skou, N. B. Jørgensen, and J. J. Arlt, Phys. Rev. Lett. **126**, 230404 (2021).
- [50] D. S. Petrov and G. E. Astrakharchik, Phys. Rev. Lett. **117**, 100401 (2016).
- [51] T. Ilg, J. Kumlin, L. Santos, D. S. Petrov, and H. P. Büchler, Phys. Rev. A **98**, 051604(R) (2018).
- [52] V. N. Popov, Theor. Math. Phys. **11**, 565 (1972).
- [53] K. Maki and X. Zotos, Phys. Rev. B **28**, 4349 (1983).
- [54] L. Allen, M. W. Beijersbergen, R. J. C. Spreeuw, and J. P. Woerdman Phys. Rev. A **45**, 8185 (1992).
- [55] V. Garcés-Chávez, D. McGloin, H. Melville, W. Sibbett, and K. Dholakia, Nature **419**, 145 (2002).
- [56] S. W. Hell, Nature Methods **6**, 24 (2009).
- [57] C. Hnatovsky, V. Shvedov, W. Krolikowski, and A. Rode, Phys. Rev. Lett. **106**, 123901 (2011).
- [58] U. R. Fischer and G. Baym, Phys. Rev. Lett. **90**, 140402 (2003).
- [59] M. N. Tengstrand, P. Stürmer, E. Ö. Karabulet, and S. M. Reimann, Phys. Rev. Lett. **123**, 160405 (2019).
- [60] R. Dubessy, T. Liennard, P. Pedri, and H. Perrin, Phys. Rev. A **86**, 011602(R) (2012).
- [61] A. Ramanathan, K. C. Wright, S. R. Muniz, M. Zelan, W. T. Hill, III, C. J. Lobb, K. Helmer-son, W. D. Phillips, and G. K. Campbell, Phys. Rev. Lett. **106**, 130401 (2011).
- [62] B. E. Sherlock, M. Gildemeister, E. Owen, E. Nugent, and C. J. Foot Phys. Rev. A **83**, 043408 (2011).
- [63] Y. Guo, R. Dubessy, M. de Gorède Herve, A. Kumar, T. Badr, A. Perrin, L. Longchambon, and H. Perrin, Phys. Rev. Lett. **124**, 025301 (2020).